Journal of The Electrochemical Society, **154** (1) A34-A38 (2007)
0013-4651/2006/154(1)/A34/5/$20.00 © The Electrochemical Society

Study on Pseudocapacitance Mechanism of Aqueous $MnFe_2O_4$ Supercapacitor

Shin-Liang Kuo,[a] Jyh-Fu Lee,[b] and Nae-Lih Wu[a,*,z]

[a]*Department of Chemical Engineering, National Taiwan University, Taipei, Taiwan*
[b]*National Synchrotron Radiation Research Center, Hsinchu 300, Taiwan*

The electrochemical mechanism leading to the pseudocapacitance of $MnFe_2O_4$ in aqueous electrolyte solutions has been investigated by, in addition to electrochemical characterization, synchrotron X-ray absorption near-edge spectroscopy (XANES) and X-ray diffraction (XRD) analyses using KCl solution as the model electrolyte. The ferrite crystallites, prepared by a solution method, contain Mn and Fe ions randomly distributed over the tetrahedral and octahedral sites of the spinel structure and exhibit an average capacitance exceeding 100 F/g-ferrite. Based on the data from the in situ XANES and XRD measurements and open-circuit-potential dependence on solution pH, it is concluded that the pseudocapacitance of $MnFe_2O_4$ involves charge transfer at both the Mn- and Fe-ion sites, balanced by insertion/extraction of proton into/from the lattice. In addition, compared with $MnO_2{\cdot}nH_2O$ electrode, the ferrite exhibits a far reduced, by ~90%, lattice expansion upon cycling.
 [DOI: 10.1149/1.2388743]

Manuscript submitted June 7, 2006; revised manuscript received August 28, 2006. Available electronically November 21, 2006.

Supercapacitors can be divided into two categories, depending on their charge-storage mechanism. The first category is referred to as the electric double layer capacitor (EDLC), of which capacitance arises from charge storage electrostatically at the interfaces between the electrodes and electrolyte solution.[1-4] The second category is the so-called pseudocapacitor, which involves faradaic reactions but behaves like a capacitor rather than a galvanic cell.[5-16] The pseudocapacitors typically exhibit a capacitance-per-unit surface area of the electrode material that is more than 10 times that of the EDLCs.

There have been known several transition metal oxides that exhibit pseudocapacitance in aqueous electrolyte. For instance, the pseudocapacitance of hydrous RuO_2[8,9,17] is known to arise from successive multielectron transfer at Ru ion sites, from, e.g., Ru^{+4} to Ru^{+3}, then to Ru^{+2}, balanced by the insertion of a proton along with different amounts of water molecules.[17] There is a continuously variable degree of oxidation/reduction, leading to the capacitor behavior. Hydrated amorphous or nanocrystalline manganese oxide, $MnO_2{\cdot}nH_2O$[11,18,19] is another pseudocapacitive material that has recently drawn much research interest. This material exhibits pseudocapacitance in solutions of several alkali salts, such as LiCl, NaCl, and KCl. Its pseudocapacitance is known to arise from electron transfer at the Mn ion sites, and the charge transfer was once suggested to be balanced either by chemisortion/desorption of electrolyte cations[18] or by insertion/extraction of protons.[19] Our recent work using electrochemical quartz-crystal microbalance (EQCM) and in situ synchrotron X-ray analyses, however, has indicated that the reaction involves bulk insertion/extraction of both oxonium (H_3O^+) and electrolyte cation.[20] Up to ~2.5% in lattice expansion when cycled within an operation potential window of 1 V has been detected, and this may be the main cause of the poor cycling stability exhibited by this material. In contrast to the lattice cation-driven mechanism, Fe_3O_4 exhibits pseudocapacitance in aqueous solutions of alkali sulfite salts, and the charge storage arises from redox reactions of the specifically adsorbed electrolyte anion, namely sulfite (SO_3^{-2}).[21]

We have recently reported[22] that some crystalline ferrite oxides, particularly $MnFe_2O_4$ and $CoFe_2O_4$, also exhibited pseudocapacitance in aqueous solutions of alkali/alkaline chlorides and sulfates. In the present work, the redox mechanism associated with the pseudocapacitance of $MnFe_2O_4$ in a model electrolyte, $KCl_{(aq)}$, has been studied. In brief, by using in situ X-ray absorption near-edge spectroscopy (XANES) and X-ray diffraction (XRD) analyses, it is established that the pseudocapacitance of $MnFe_2O_4$ involves charge transfer at both the Mn- and Fe-ion sites over different potential ranges, balanced by insertion/extraction of proton into/from the lattice. The reaction leads to a lattice expansion by ~0.25%, which is nearly one-tenth that of $MnO_2{\cdot}nH_2O$.

Experimental

$MnFe_2O_4$ was studied in a composite powder form which contains $MnFe_2O_4$ and carbon black (CB, Vulcan XC72, Cabot Corporation) with a 1:1 weight ratio. The CB helps to increase the overall electronic conductivity of the powder and also serves as an electrolyte reservoir for improving high-rate performance.[22] The composite powder was prepared by a coprecipitation method in alkaline aqueous solutions as follows. $MnSO_4$ was dissolved along with $FeCl_3$ with a stoichiometric ratio of 1:2 in 1 M HCl aqueous solution with bubbling N_2, followed by adding the predetermined amount of CB powder. The solution is then added into another solution that contains 1.5 M NaOH under vigorous stirring. Black precipitate was formed immediately upon mixing. It was found that the CB particles sedimented simultaneously with the oxide precipitate, suggesting that the oxide component was homogeneously combined with the CB particles during the synthesis process. The supernatant liquid was then decanted and fresh deionized water was added. Repeated solution-decanting and water-replenishing processes were carried out to remove residual anions. Finally, the powder was dried in air at 50°C, followed by calcination at 350°C, unless otherwise specified, for 2 h in N_2.

For electrochemical characterization, supercapacitor electrodes were made of the ferrite/CB composite powder, polyvinylidene fluoride (PVdF) in 10 wt % and Ti foil as current collector, and they were finally dried at 120°C for 6 h in vacuum. Electrochemical characterizations were carried out with a three-electrode cell with Pt mesh and Ag/AgCl/saturated KCl [EG&G, 197 mV vs normal hydrogen electron (NHE) at 25°C] as the counter and reference electrodes, respectively. The potentials mentioned hereafter are based on this reference electrode. Symmetric cell configuration having one of the two identical composite electrodes as the reference was also adopted for cycling tests. The electrolyte solution was 1 M KCl aqueous solution, unless it is otherwise specified. Cyclic voltammetry (CV) curves were recorded by an electrochemical analyzer (Eco Chemie PGSTAT30). The average specific capacitance of the electrodes was calculated by

$$C_{\text{avg}} = \Delta Q/w\Delta V = \left(\int IdV\right)/s/\Delta V/w \qquad [1]$$

where ΔQ is the total amount of charge accumulated over a potential window ΔV, w is the mass of active material in an electrode, I is the current, and s is the potential scan-rate.

Synchrotron XRD and XANES measurements were conducted, respectively, at beam lines 01C2 and 17C1 of the National Synchro-

* Electrochemical Society Active Member.
z E-mail: nlw001@ntu.edu.tw

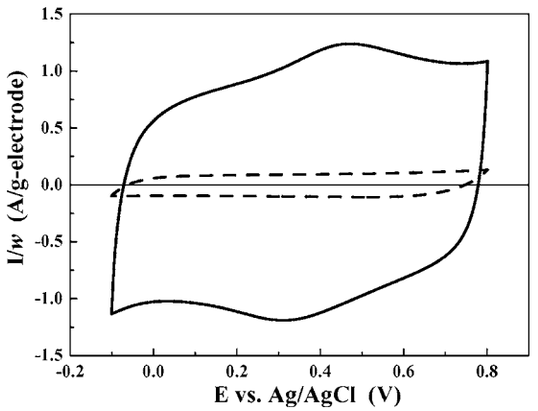

Figure 1. Voltammograms of the (solid line) $MnFe_2O_4$–CB composite and (dashed line) pure CB electrodes in 1 M KCl electrolyte. The potential scan-rate is 20 mV/s. The curves have been normalized to have the same amount of CB.

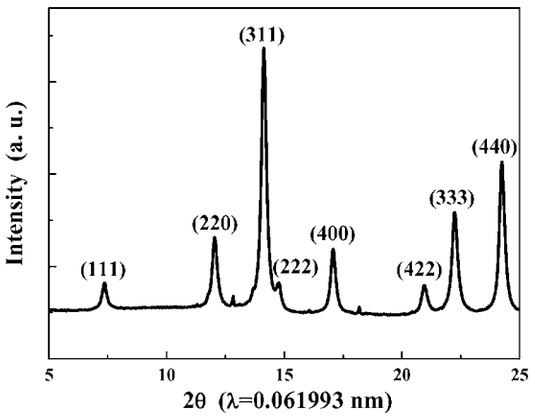

Figure 2. XRD pattern of the $MnFe_2O_4$ composite. The (*h k l*) indexation is based on Jacobsite $MnFe_2O_4$.

tron Radiation Research Center (NSRRC) in Taiwan. For the in situ measurements, the electrodes used Ti mesh as the current collector with poly(tetrafluoroethlene) (PTFE) as the binder. The electrochemical cell was made of acrylics, and the two opposite walls of the cell were perforated and then sealed with Kapton films in order to allow the X-ray beam to pass through the cell without excessive attenuation. For in situ XANES experiment, CV was run at a scan rate of 0.2 mV/s, and the scan was interrupted at each selected potential for 10 min for data collection. For the in situ XRD, CV was run at the same speed, and the patterns were recorded with a translating curved imaging plate (Fuji BAS2500) with a sample-to-film distance of 280 mm. Two-dimensional data were converted using the FIT2D program.

Results and Discussion

Electrochemical characterization.— Figure 1 shows the CV curve of the composite powder electrode in 1 M KCl at a potential scan rate of 20 mV/s. For comparison, the voltammogram from a pure CB electrode was also shown, and the current has been normalized to have the same weight (50% by weight) as in the composite powder electrode. The comparison indicates that the CB component is expected to contribute no more than 9% of the capacitance of the composite powder electrode (some CB surface may even be blocked by the ferrite particles in the composite). The CV curve of the composite powder electrode is not perfectly rectangular but exhibits redox humps between 0.2 and 0.6 V. The average specific capacitance as calculated by Eq. 1 is 63.4 F/g. Subtracting the maximum contribution of the CB component ($\sim$5 F/g) gives a specific capacitance of $\sim$115 F/g for the ferrite component.

Material characterization.— The XRD pattern of the composite powder shows reflection peaks that are consistent with face-centered cubic spinel structure (Fig. 2). The calculation using the Scherrer equation based on the full-width at half-maximum intensity of the (311) reflection gives an average crystallite size of 13.2 nm. It has been confirmed by transmission electron microscopy (not shown) that the crystallites are homogeneously dispersed on the surfaces of CB particles.

The Mn and Fe K-edge XANES spectra of the composite powder were shown in Fig. 3. Spectra of some standard samples were also shown for comparison. Each XANES spectrum can be further divided into a pre-edge region A (e.g., for Mn: 6537–6545 eV) containing weak peaks, a main edge region B (for Mn:6545–6555 eV), and resonance peak regions C (for Mn: 6555–6566 eV) and D (for Mn: 6566–6580 eV).[23-25] The peaks within pre-edge region A are ascribed to 1s $\rightarrow$ 3d transitions.[23] The main absorption region B can be assigned[23,25] to the transition from 1*s* to *p*-like states of t_{1u} symmetry. The associated edge energy is conventionally taken as the energy at the first inflection point. The edge energy is known to increase with increasing valence of the transition metal ion within the oxides.[23-25] Compared with the curves of the standard samples, the average valences of both Mn and Fe in the composite powder are found to be quite close to +3. They are consistent with the theoretical average valence, 2.67, of the metal ions.

The regions C and D and the region beyond are sensitive to site symmetry as well as multiscattering resonance of the photoelectron

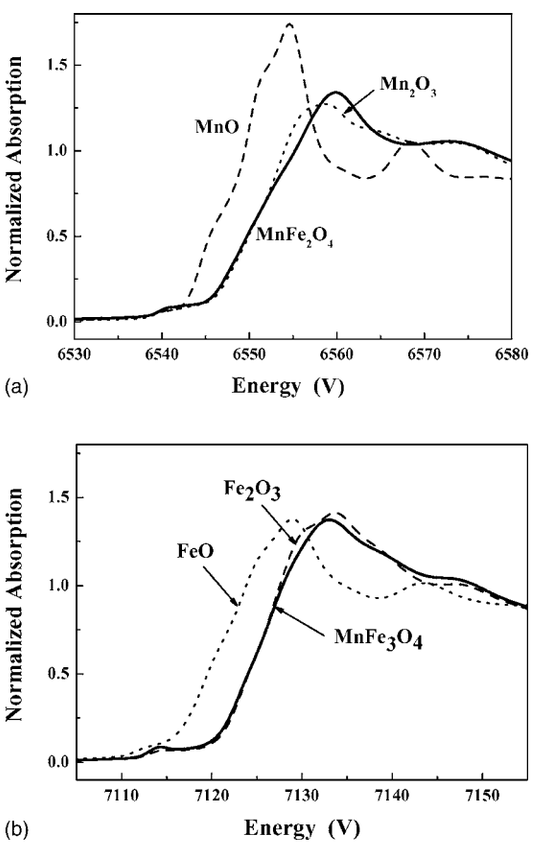

Figure 3. Normalized XANES spectra for $MnFe_2O_4$: (a) Mn K-edge, in comparison with MnO and Mn_2O_3, and (b) Fe K-edge, in comparison with Fe_2O_3.

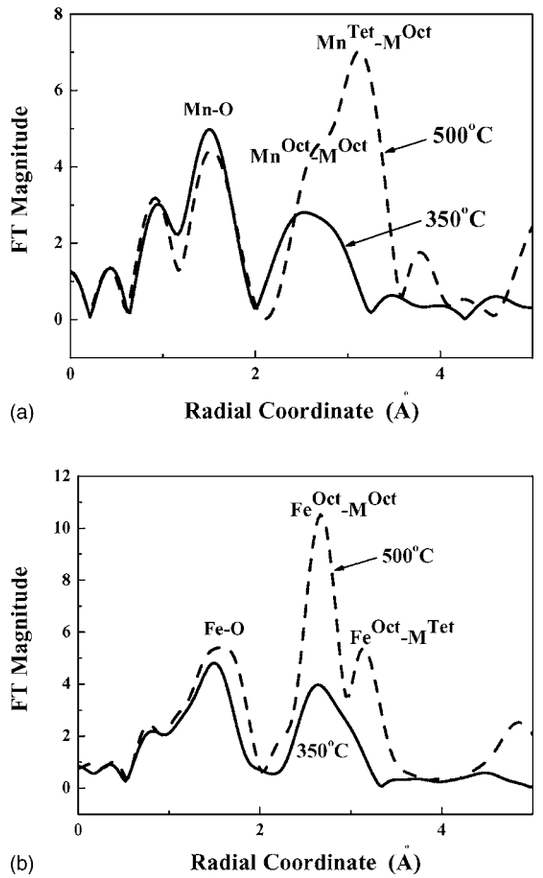

Figure 4. Fourier transforms of k^3-weighted EXAFS spectra of the $MnFe_2O_4$ composite electrode calcined at (solid line) 350 and (dashed line) 500°C: (a) Mn K-edge and (b) Fe K-edge.

by neighboring atoms.[26] Structural information of neighboring atoms can be obtained by analyzing the extended region (extended X-ray absorption fine structure, EXAFS) up to 1000 eV above the main absorption edge energy. The Fourier-transformed k^3-weighted Mn and Fe K-edge EXAFS data of the composite powder were presented in Fig. 4. For comparison, spectra acquired from the composite powder calcined at 500°C, which is better crystallized, were also shown.

In the ferrite structure, two distinct spatial arrangements of cation sites are involved, namely tetrahedral (Tet) and octahedral (Oct) sites. The Tet-site cations have four nearest O neighbors, forming MO_4 tetrahedron, followed by 12 cations at Oct sites. Each Oct site cation is surrounded by six nearest O neighbors, the second shell of 6 Oct-site cations, and the third shell of Tet-site cations. The third shell coordination of the Oct site (i.e., Oct–Tet coordination) coincides with the second shell of the Tet site (Tet–Oct coordination). The Fourier-transformed spectra (Fig. 4) basically shows the radial distribution function of the local atomic environment around the absorbing element. Without phase correction, the present radial distance shows a deviation around −0.3 Å from the real interatomic distance. The coordination shells discussed above are clearly shown for the 500°C calcined powder in Fig. 4. Beyond the first coordination shell of oxygens, the Mn K-edge spectrum of the 500°C powder shows an Oct–Oct coordination peak (shoulder), followed by a stronger peak ascribed to Tet–Oct plus Oct–Tet coordination. The Fe spectrum exhibits essentially the same peak sequence except that the Oct–Oct coordination peak has a much stronger intensity than the Tet–Oct (plus Oct–Tet) peak. The intensity difference indicates that in the 500°C powder, the octahedral sites are predominantly occupied by Fe ions, while Mn ions mainly occupy the tetrahedral sites.

For the 350°C calcined powder, the intensities of the metal–metal coordination peaks decreased dramatically (Fig. 4) in both the Mn and Fe spectra. In addition, both the Oct–Oct and Tet–Oct peaks shifted to lower radial distances. Similar effects have also been observed for other low-temperature calcined powders in the literature, and they were suggested to partly arise from lattice disorder.[27] That is, the 350°C calcined ferrite contains significantly more lattice defects than the 500°C powder. Moreover, the change in the intensity ratios between the Oct–Oct and Tet–Oct peaks suggests different distribution of cations over the Tet and Oct sites in the 350°C powder from in the 500°C powder. Zhang et al.,[28] employing neutron diffraction combined with electron energy loss analysis, studied the effect of heat treatment on the cation distribution of $MnFe_2O_4$ prepared by a similar solution method to the present study. They found that the distribution of the Mn ions varied with increasing heat-treatment temperature from being random to predominantly at the tetrahedral site, while the average valence of Mn concurrently changed from nearly +3 toward +2. Accordingly, taking the present XANES and EXAFS data together into account, it is concluded that Mn cations in the 350°C calcined powder are randomly distributed over the octahedral and tetrahedral sites with a valence close to the theoretical average valence, +2.67.

In situ studies.— To monitor the valence change of cations of the ferrite, XANES spectra at Mn and Fe K-edges were recorded during the CV scan between 0.8 and −0.1 V (vs Ag/AgCl). It was found that for both Mn and Fe K-edges, while the overall shape of the spectrum profiles did not change, the absorption edge front of the probed metal ions shifted back and forth with variation in applied potential. Figure 5 shows the spectra taken during a cathodic scan, in which the absorption edges for both Mn and Fe ions shift toward lower energies with decreasing potential. In Fig. 6, it is interesting to note that the edge energy of the Mn decreases monotonically with decreasing potential. The edge energy and hence the valence of the Fe ion decreases with reduction only within the potential window from 0.5 to 0.1 V. This potential range is the region where the redox hump takes place in the CV curve (Fig. 1). Therefore, it is concluded that the charge transfer at the Mn-ion sites contributes to the capacitor-like component of the current curve, while that at the Fe ions causes the battery-like component. Both components are completely reversible.

In situ XRD study was conducted to monitor the lattice variation along the course of charge–discharge cycling. The reflections of the Ti current collector can be taken as the internal standards. The entire set of the peaks of the ferrite were also seen to shift back and forth upon CV cycling. An example is shown in Fig. 7, where it is shown that the (311) reflection peak shifts toward a lower angle during the cathodic scan, suggesting lattice expansion, and then back to the original positions during the anodic scan. The structural variation is completely reversible. The overall extent of lattice variation between 0.9 and −0.1 V is 0.25%, which is equivalent to 1.04% per mole of electron transferred. This is only one-tenth of that (~10%) of the hydrated $MnO_2 \cdot nH_2O$ electrode.[21] The small volume expansion exhibited by the ferrite is expected to enhance high-rate cycling stability of electrode.

Open-circuit potential.— The open-circuit potential (OCP) of the composite powder electrode was measured as a function of pH value in a 1 M KCl solution. The pH value of the solution was increased stepwise with an increment ΔpH of ~0.5, and the OCP was taken 30 min after the pH change. As shown in Fig. 8, the OCP-pH correlation gives a slope, dE/dpH, of −52.4 mV within pH range between 6 and 9.

Mechanism.— The operating potential window of $MnFe_2O_4$ is very different from that of the Fe_3O_4 electrode in the aqueous sulfite-containing electrolyte solution.[21] Rather, it is very similar to the potential window of $MnO_2 \cdot nH_2O$ in the alkali chloride electro-

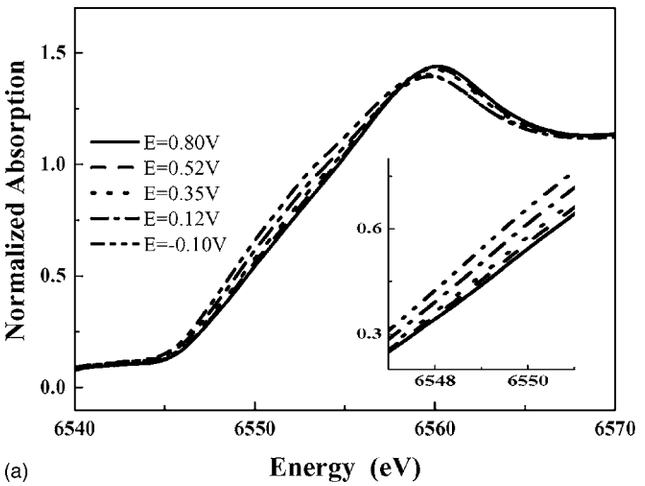

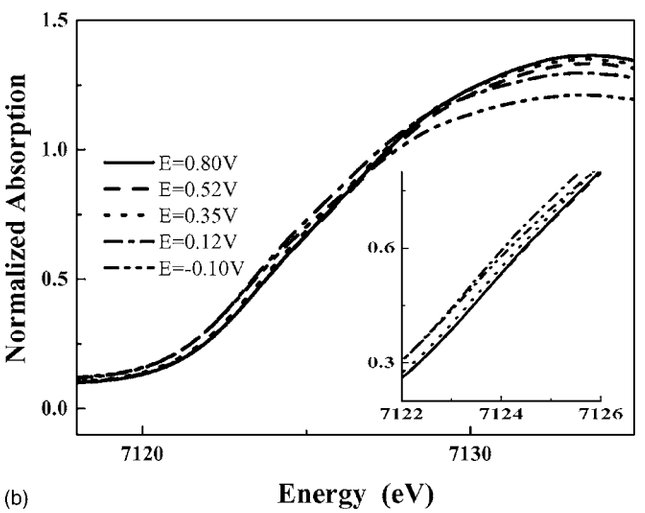

Figure 5. (a) Mn K-edge and (b) Fe K-edge XANES spectra taken in situ along a cathodic scan in 1 M KCl aqueous electrolyte.

lyte solutions.[11,18] The present XANES data have clearly indicated that the redox reactions of the composite powder electrode involve electron transfer at both the Mn and Fe ions of $MnFe_2O_4$. The OCP data, which show a pH dependence, dE/dpH, of −52.4 mV, suggested that the reaction may involve H^+ either with or without association with water molecule(s). In our recent study on the hydrated $MnO_2{\cdot}nH_2O$ thin-film electrode by EQCM in alkali salt solutions,[21] it was established that the pseudocapacitance mechanism for $MnO_2{\cdot}nH_2O$ involves bulk insertion of predominantly H_3O^+, which also gives similar pH dependence for OCP. Unfortunately, it has not yet been successful in preparing $MnFe_2O_4$ thin film for similar EQCM analysis. However, the ferrite has exhibited a reversible lattice expansion which is merely one-tenth of that of $MnO_2{\cdot}nH_2O$.[21] It thus may be argued that, for the $MnFe_2O_4$ supercapacitor, the inserting proton species is not likely associated with any water molecule. The difference may be related to the fact that the ferrite phase is a crystalline material, in contrast to the nearly amorphous nature of the MnO_2 electrode. The latter could have a more open structure, capable of accommodating larger inserting cations, such as hydrated proton and alkali cations.[21] In addition, the

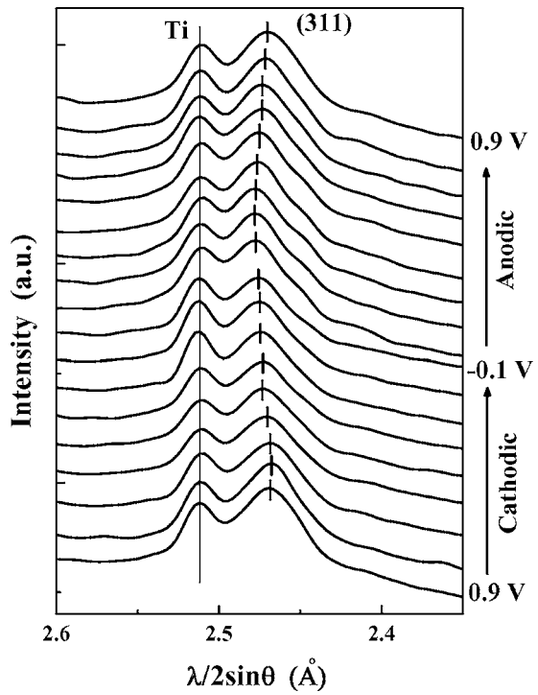

Figure 7. In situ synchrotron XRD patterns of the $MnFe_2O_4$ composite electrode acquired during CV cycling in 1 M KCl solution.

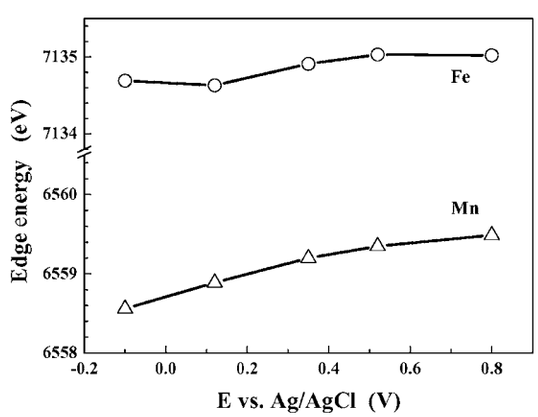

Figure 6. Evolution of edge energy on Mn and Fe of $MnFe_2O_4$ as a function of potential.

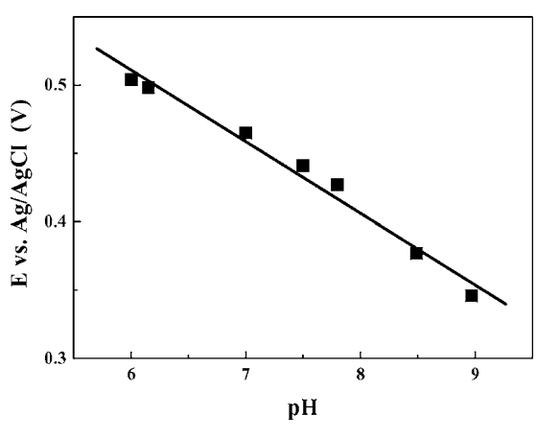

Figure 8. OCP of the $MnFe_2O_4$ composite electrode vs pH in a 1 M KCl electrolyte.

specific surface area ($<75\ m^2/g$) of the ferrite crystallites is too small to assume that the pseudocapacitance is restrictively a superficial process. Accordingly, the overall electrochemical reaction should be written as

$$\delta Mn^{+3} + (1 - \delta)Fe^{+3} + H^+_{(aq)} + e^- \rightarrow \delta Mn^{+2} + (1 - \delta)Fe^{+2} + H^+_{(lattice)} \quad [2]$$

Conclusion

The pseudocapacitive charge storage reactions of crystalline $MnFe_2O_4$ in aqueous KCl solutions have been investigated. By using in situ XANES and XRD analyses, it was established that the redox reaction of the ferrite phase involves charge transfer at both the Mn and Fe ions over different potential ranges, balanced by insertion/extraction of proton into/from the lattice. The redox reaction involves a very small lattice expansion ($\sim 0.25\%$ over an operation potential window of 1 V), which can enable high-rate cycling stability for this supercapacitor.

Acknowledgment

This work is supported by National Science Council of Republic of China under contract no. NSC 94-2214-E-002-003.

National Taiwan University assisted in meeting the publication costs of this article.

References

1. B. E. Conway, *J. Electrochem. Soc.*, **138**, 1539 (1991).
2. S. Sarangapani, B. V. Tilak, and C.-P. Chen, *J. Electrochem. Soc.*, **143**, 3791 (1996).
3. D. C. Grahame, *Chem. Rev. (Washington, D.C.)*, **41**, 441 (1947).
4. M. A. V. DeVanathan and B. V. Tilak, *Chem. Rev. (Washington, D.C.)*, **65**, 635 (1965).
5. S. Trasatti and G. Buzzanca, *J. Electroanal. Chem. Interfacial Electrochem.*, **29**, 1 (1971).
6. L. D. Burke, O. J. Murphy, J. F. O'Neill, and S. Venkatesan, *J. Chem. Soc., Faraday Trans. 1*, **73**, 1659 (1977).
7. B. E. Conway, V. Birss, and J. Wojtowicz, *J. Power Sources*, **66**, 1 (1997).
8. J. P. Zheng and T. R. Jow, *J. Electrochem. Soc.*, **142**, L6 (1995).
9. J. P. Zheng, P. J. Cygan, and T. R. Jow, *J. Electrochem. Soc.*, **142**, 2699 (1995).
10. T. R. Jow and J. P. Zheng, *J. Electrochem. Soc.*, **145**, 49 (1998).
11. H. Y. Lee and J. B. Goodenough, *J. Solid State Chem.*, **144**, 220 (1999).
12. H. Y. Lee and J. B. Goodenough, *J. Solid State Chem.*, **148**, 81 (1999).
13. N. L. Wu, Y. P. Lan, C. Y. Han, S. Y. Wang, and L. R. Shiue, in *Electrochemical Capacitor and Hybrid Power Sources*, R. J. Brodd, D. H. Doughty, J. H. Kim, M. Morita, K. Naoi, G. Nagasubramanian, and C. Nanjundiah, Editors, PV 2002-7, p. 95, The Electrochemical Society Proceedings Series, Pennington, NJ (2002).
14. N. L. Wu, S. Y. Wang, C. Y. Han, D. S. Wu, and L. R. Shiue, *J. Power Sources*, **113**, 173 (2003).
15. S. Y. Wang and N. L. Wu, *J. Appl. Electrochem.*, **33**, 345 (2003).
16. L. R. Shiue, N. L. Wu, D. S. Wu, C. W. Chao, and Y. P. Lan, U.S. Pat. 6,678,147 (2004).
17. M. C. Santos, A. J. Terezo, V. C. Fernandes, E. C. Pereira, and L. O. S. Bullhões, *J. Solid State Electrochem.*, **9**, 91 (2005).
18. H. Y. Lee, V. Manivannan, and J. B. Goodenough, *C. R. Acad. Sci, Paris, Ser. IIC: Chim*, 565 (1999).
19. S-C. Pang, M. A. Anderson, and T. W. Chapman, *J. Electrochem. Soc.*, **147**, 444 (2000).
20. S. L. Kuo and N. L. Wu, *J. Electrochem. Soc.*, **153**, A1317 (2006).
21. S. Y. Wang, K. C. Ho. S. L. Kuo, and N. L. Wu, *J. Electrochem. Soc.*, **153**, A75 (2006).
22. S. L. Kuo and N. L. Wu, *Electrochem. Solid-State Lett.*, **8**, A495 (2005).
23. M. Belli, A. Scafati, A. Bianconi, S. Mobilio, L. Palladino, A. Reate, and E. Burattini, *Solid State Commun.*, **35**, 355 (1980).
24. B. Ammundsen, D. J. Jones, and J. Roziere, *J. Solid State Chem.*, **141**, 294 (1998).
25. N. Y. Safontseva and I. Y. Nikiforov, *Phys. Solid State*, **43**, 61 (2001).
26. R. S. Liu, L. Y. Jang, J. M. Chen, Y. C. Tsai, Y. D. Hwang, and R. G. Liu, *J. Solid State Chem.*, **128**, 326 (1997).
27. E. E. Carpenter, C. J. O'Connor, and V. G. Harris, *J. Appl. Phys.*, **85**, 5175 (1999).
28. Z. J. Zhang, Z. L. Wang, B. C. Chakoumakos, and J. S. Yin, *J. Am. Chem. Soc.*, **120**, 1800 (1998).